J Mater Sci (2024) 59:10003–10021

Lightweight Materials

Hot compression deformation characteristics of TiBw/Ti65 composites for high-temperature application

Shaocong Xiong[1], Qi An[1,*], Shuai Wang[1], Rui Zhang[1], Xin Chen[1], Run Chen[1], Lujun Huang[1,2,*], Sergey Zherebtsov[3], and Lin Geng[1,2]

[1] *School of Materials Science and Engineering, Harbin Institute of Technology, P. O. Box 433, Harbin 150001, People's Republic of China*
[2] *Stake Key Laboratory of Advanced Welding and Joining, Harbin Institute of Technology, Harbin 150001, People's Republic of China*
[3] *Belgorod State University, Belgorod 308015, Russia*

Received: 26 September 2023
Accepted: 2 January 2024
Published online:
27 March 2024

ABSTRACT

Ti–5.9Al–4.0Sn–3.5Zr–0.5Mo–0.3Nb–1.0Ta–0.4Si–0.8W–0.05C (Ti65) alloy is a high-temperature titanium alloy designed for service at 650 °C. To further improve the elevated temperature mechanical performance of Ti65, Ti65-based composites have been fabricated in the present study through a low-energy ball milling and reaction hot-press sintering process. Hot compression tests were further performed on the as-sintered TiB/Ti65 composites at the temperature ranging from 1040 to 1100 °C at the strain rate of 1–0.001 s^{-1}. The results show that during deformation at 1–0.1 s^{-1}, dynamic recrystallization was the dominant mechanism. At the low strain rate of 0.01–0.001 s^{-1}, dynamic recovery became the predominant mechanism. Hyperbolic constitutive equations were calculated and the processing maps were constructed based on dynamic material modeling. The activation energy for hot deformation was determined to be 321.57 kJ/mol and the ideal processing parameters for the network composite were 1070–1100 °C with a strain rate of 1–0.1 s^{-1}. The microstructural analysis of the hot compression-deformed samples revealed the presence of two dynamic recrystallization mechanisms: continuous dynamic recrystallization and discontinuous dynamic recrystallization. After hot compression, metallic matrix exhibited preferred orientation, including a strong $< \bar{1}2\bar{1}0 >$//CD fiber texture and $< 01\bar{1}1 >$//CD fiber texture. Matrix flow induced TiB whiskers rotation, producing a pronounced [100]//CD texture and a weak [010]//RD and [010]//ND texture.

Handling Editor: P. Nash.

Address correspondence to E-mail: anqi1993@hit.edu.cn; huanglujun@hit.edu.cn

https://doi.org/10.1007/s10853-024-09461-3

Introduction

Near α titanium alloys have been commonly employed as significant structural materials in aerospace, automotive and military fields due to low density, high specific strength, and excellent resistance to creep deformation [1–4]. Traditional near α titanium alloys, such as Ti–6Al–2.75Sn–4Zr–0.4Mo–0.45Si (in weight percent wt%) (Ti1100) [5], Ti–5.8Al–4Sn–3.5Zr–0.7 Nb–0.5Mo–0.35Si (IMI834) [6], Ti–6.2Al–2Sn–3.6Zr–0.7Mo–0.15Si–5 W (TB36) [7], and Ti–5.8Al–4.0Sn–3.5 Zr–0.4Mo–0.4Nb–1.0Ta–0.4Si–0.06C (Ti60) [8], exhibit favorable tensile strength and creep resistance at temperatures below 600 °C. Ti–5.9Al–4.0Sn–3.5Zr–0.5Mo–0.3Nb–1.0Ta–0.4Si–0.8W–0.05C (Ti65) alloy is a newly developed high-temperature titanium alloy with a service temperature of 650 °C [9], which is considered the highest temperature at which titanium alloys can currently be used. However, due to the limitations of aluminum equivalent, the solid solution strengthening resulting from the addition of alloying elements cannot further enhance strength of titanium alloys at elevated temperature. By introducing ceramic reinforcements into the titanium alloys, the high-temperature performance can be significantly improved, resulting in titanium matrix composites (TMCs) with higher specific strength, higher elastic modulus, and excellent heat resistance [10–13]. Notably, Huang et al. [14–20] fabricated a series of TMCs with quasi-continuous network architecture TiB whiskers (TiBw) by low-energy ball milling and hot-press sintering, exhibiting both high strength and good ambient temperature plasticity. The TiBw-rich regions bear the applied stress; while, the TiBw-lean regions contribute to plastic deformation.

The investigation of hot deformation behavior is of paramount importance for the processing and forming of a novel alloy. For instance, Li et al. [21] developed a novel Zn-0.8Mn alloy with high ductility, derived its constitutive equation, obtained the processing map for the first time, which provide scientific guidance for hot deformation processing of Zn–Mn-based alloys. As a newly developed high-temperature titanium alloy, Ti65 alloys contain a significant amount of alloying elements, which often results in higher strength [22] but relatively undesirable hot workability. Consequently, Zhang et al. [23] investigated the workability and texture evolution of Ti65 alloy, they discovered the deformation instability zone when the strain rate exceeds 0.01 s^{-1} based on the processing map. Furthermore, Zhang et al. [24] have studied the hot deformation behavior of Ti65 alloy, the results indicated that during deformation in the β phase region, dynamic recrystallization (DRX) predominated, and the variant selection of α martensite followed the Burgers orientation relationship (BOR). Simultaneously, Ti65 alloy has primarily been investigated for improving its high-temperature mechanical properties through heat treatment [9, 25–27] or hot deformation [28]. However, there is limited research on enhancing the high-temperature performance of Ti65 alloy through compositing.

Hot deformation processes, such as rolling [29–31], extrusion [32, 33], and forging [34, 35], can eliminate defects and further enhance the mechanical properties of TMCs. In addition, the introduction of ceramic reinforcements can increase the resistance to deformation but worsen its hot workability. Therefore, characterizing the microstructure evolution during hot deformation is necessary before practical usage of near α titanium alloy-based composites. Wang et al. [36, 37] investigated the hot deformation behavior and microstructural evolution of network structure TiBw/Ti60 composites. They pointed out that TiBw can act as nucleation sites during dynamic recrystallization. According to Zhang et al. [38], the feasibility of reconstructing the β-Ti through BOR was confirmed, subsequently revealing the microstructural evolution of TiBw/Ti60 composites in the single β phase region. Li et al. [39] investigated the microstructural evolution during the rolling process of network structure TiBw/Ti–6.5Al–2Zr–1Mo–1V (TA15) composites and attributed the texture formation to the rolling deformation and dynamic recrystallization. Besides, Zhang et al. [40] proposed that the reinforcement can promote the formation of some subgrains in (TiBw + TiC particle)/Ti composites during isothermal compression. Based on the above discussions, there is currently no research on flow stress behavior, constitutive equation, processing map, the matrix texture, and TiBw orientation of the network structure TiBw/Ti65 composites during hot compression deformation.

In this work, the network architecture TiBw/Ti65 composites were successfully prepared through low-energy ball milling and vacuum hot-press sintering techniques. Furthermore, the microstructure evolution of the as-fabricated TiBw/Ti65 composites during hot compression were investigated. It is believed that the results of this study can promote the engineering

application of such composites by providing insights into their hot deformation behavior.

Materials and experimental procedures

Materials

TiBw reinforced Ti65 composites were fabricated via reactive vacuum hot-press sintering technique. The volume fraction of TiBw was designed as 3.4 vol.%. The fabrication process is illustrated in Fig. 1. The Ti65 alloy powders (Ti–5.9Al–4.0Sn–3.5Zr–0.5Mo–0.3Nb–1.0Ta–0.4Si–0.8W–0.05C) with an average particle size of 115 μm were utilized, along with TiB_2 powders with an average particle size of 3.4 μm. Besides, 2 wt.% TiB_2 was added to the composite powder. Under the protective atmosphere of argon gas, a low-energy ball milling process (5 h at a speed of 220 rpm, ball-to-powder weight ratio of 5:1) was employed to embed the small-sized TiB_2 particles onto the surface of the larger-sized spherical titanium powder. Stainless steel balls were used during the ball milling process with a diameter of 10 mm and 6 mm with a weight ratio of 1:3. For every hour of ball milling, pause for 15 min to prevent overheating of the powder. Subsequently, the mixed powders were heated at 1300 °C in the graphite mold for 2 h with the pressure of 25 MPa. The heating rate employed during the sintering process is 10 °C/min. At the end of heating, the samples were slowly cooled in the vacuum furnace. The Ti65 powders reacted with TiB_2 powders and TiB were in situ synthesized according to Eq. (1):

$$Ti(s) + TiB_2(s) = 2TiB(s) \quad (1)$$

The β transition temperature (β_T) of the TiBw/Ti65 composites was determined to be 1040 °C using differential scanning calorimetry (DSC) and metallographic method.

Hot compression test

The high-temperature compression tests were carried out on the Gleeble 1500D dynamic thermomechanical simulator in the temperature range 1040–1100 °C with 20 °C intervals and strain rate of 0.001–1 s^{-1} with

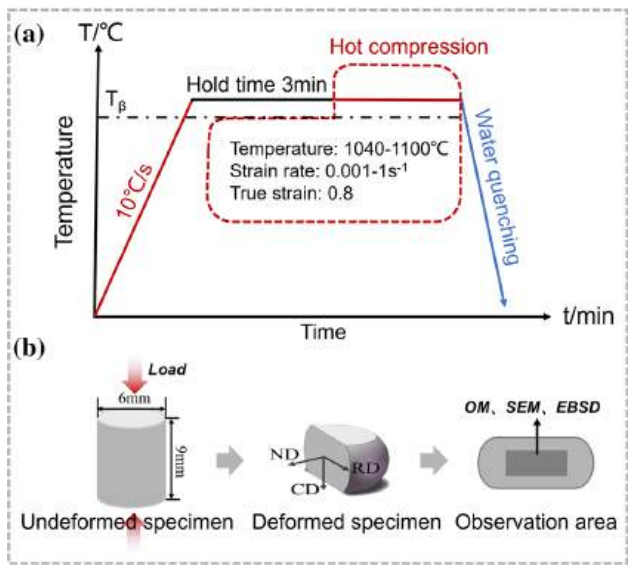

Figure 2 Schematic diagram of the hot compression test (**a**) and the compression sample (**b**).

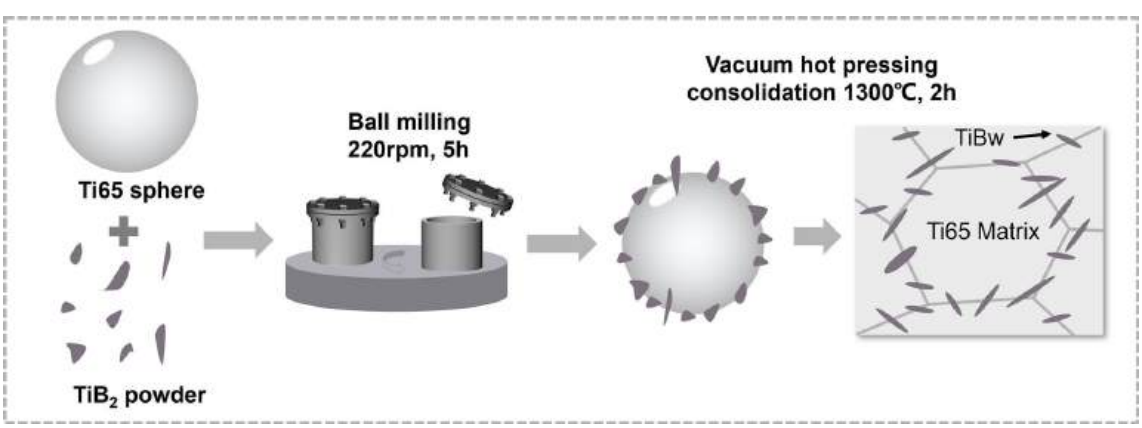

Figure 1 The schematic diagram of the fabrication process of TiBw/Ti65 composites with network architecture

0.8 true strain, as illustrated in Fig. 2a. The compression samples were cylindrical with dimensions of Φ6 mm × 9 mm, as plotted in Fig. 2b. To accurately control the sample temperature during compression, two thermocouples were welded on the side surface of the cylinder at the middle position prior to the experiment. Additionally, the graphite flakes were placed between the face of the specimen and anvils to reduce friction. Prior to the beginning of the test, the chamber was evacuated to prevent oxidation of the specimen during compression with a vacuum of less than 10^{-2} Pa. The temperature was ramped up to the designated value at a rate of 10 °C/s, followed by a 3-min isothermal hold. After deformation, the sample was rapidly water-quenched to retain the high-temperature deformation microstructure.

Microstructure characterization

Microstructural characteristics were observed using SUPRA55 scanning electronic microscopy (SEM). The phases of the composite were determined by X-ray diffraction (XRD, Panalytical X'PERT) with Cu-K_α radiation, scanning speed of 6°/min and in the range of 20°–90° (2θ). The crystallographic orientation information of the samples was obtained using electron backscattered diffraction (EBSD) technique in a section containing the compression direction (CD) and radial directions (RDs) of the deformed samples as shown in Fig. 2b. After the wire electrical discharge machining (WDEM) cutting, the samples were grinded with sandpapers up to 2000#. Subsequently, electrolytic polishing was performed at 35 V for 40 s to further remove surface scratches and stress layers. The electrolytic polishing solution consisted of $HClO_4$:$CH_3(CH_2)_3OH$:CH_3OH in a volume ratio of 1:6:10. The EBSD information were processed with the Aztec-Crystal software.

Results and discussion

Microstructure of the as-sintered TiBw/Ti65 composites

The morphology of the initial matrix alloy powder and the ball-milled composite powder is shown in Fig. 3a, b, and it can be observed that the composite powders deform slightly and still maintain a high degree of sphericity, which are mainly attributed to the low-energy ball milling. Also under this ball milling process parameter, it is able to make the

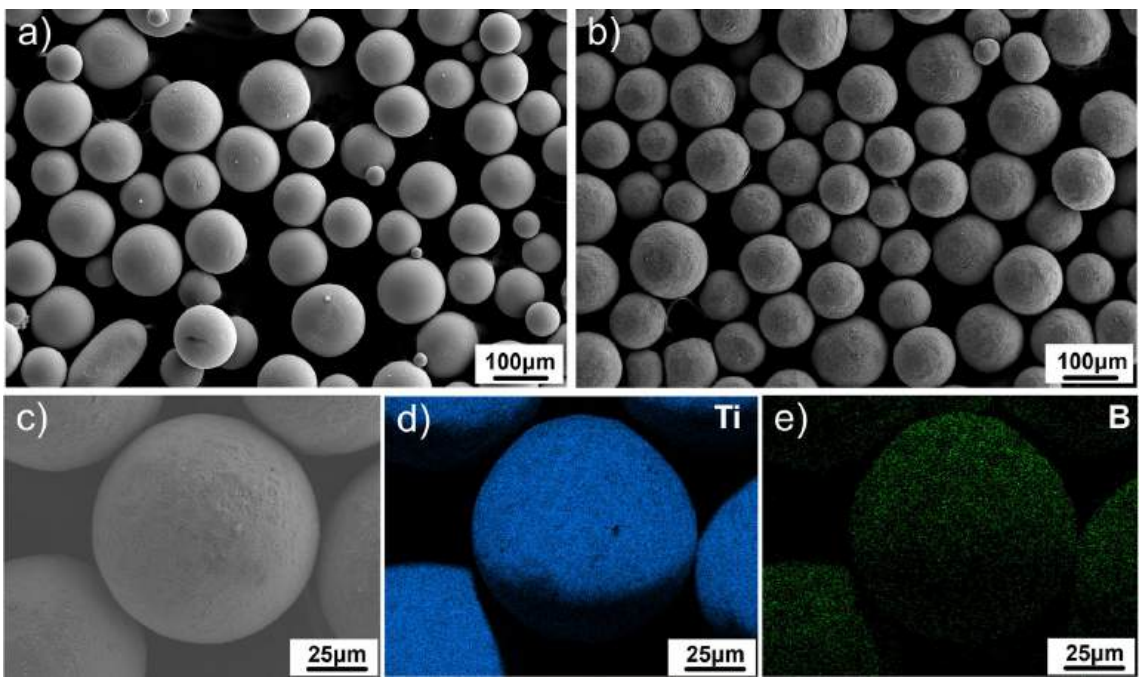

Figure 3 Morphologies of the Ti65 powders before (**a**) and after milling (**b**) and the milled powders (**c**) along with corresponding EDS mappings (**d**, **e**) of Ti, B.

small-sized TiB_2 ceramic phase uniformly embedded on the surface of Ti65 alloy powder, as shown in Fig. 3c–e. This facilitates the preparation of network-like structural composites by in situ reaction.

The microstructure of the TiBw/Ti65 composites is shown in Fig. 4. The XRD pattern in Fig. 4a demonstrates that the phases of as-sintered composite are predominantly α-Ti, β-Ti and TiBw. The added TiB_2 particles reacted with the Ti65 matrix to form TiBw, which were distributed at the interfaces of the original titanium powders. It is clearly observed that the TiBw exhibit a quasi-continuous network-like distribution in Fig. 4b. Moreover, the Ti65 matrix is interconnected at the network-like interfaces. Since Ti65 is a near α titanium alloy, the addition of a large number of α-stabilizing elements (e.g., Al) and small amount β-stabilizing elements (e.g., Mo, Nb, Ta, Si) results in a low β phase content in the microstructure at room temperature. During the slow furnace cooling process, lamellar phases (α-Ti) and intergranular phases (β-Ti) in matrix formed α/β lath, making up a basket-weave microstructure [41].

Figure 4c displays the IPF color map of α phase and the average α grain size has been measured to be approximately 21 μm. In the TiBw-enriched region, α-Ti exhibits a fine, nearly equiaxed structure, while in the TiBw-lean region, α-Ti are coarse and lamellar. The α grain size in the TiBw-enriched region is smaller than that in the TiBw-lean region, forming a bimodal microstructure resembling fine grains enveloping coarse grains. This is due to the fact that during furnace cooling, the TiBw at the network interfaces can serve as nucleation sites for the precipitation of the α-Ti [42, 43]. Besides, during slow furnace cooling processes, a solid-state phase transformation occurs where β-Ti is transformed into α-Ti. The interfacial energy between the two phases decreases with the increase in the matching degree of the atomic arrangement on both sides of the interface, and the lowest total surface energy is always desired during nucleation, so the identified specific ORs and excellent lattice matches between α-Ti and TiB aid in this heterogeneous nucleation of α-Ti [44]. According to the BOR, the reconstruction of the parent β phase is shown in Fig. 4e. Comparing with the position of TiBw in

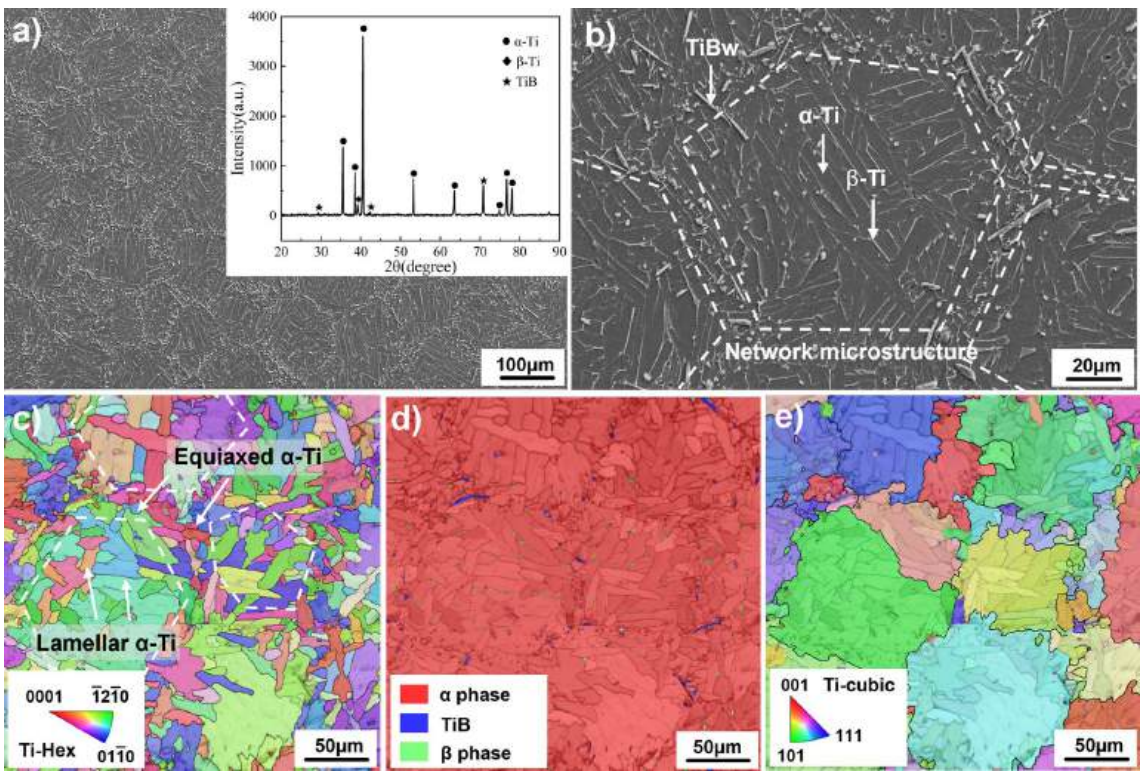

Figure 4 Microstructure of the as-sintered TiBw/Ti65 composites with network architecture: **a** low magnification SEM-SE micrograph and X-ray diffraction pattern; **b** high magnification SEM-SE micrograph; **c** the IPF color map of α phase; **d** the phase map of the composite; **e** the reconstructed β phase.

Fig. 4d, it can be observed that the TiBw effectively restrict the growth of the β phase at high temperature, confining the high-temperature β phase within a network unit (approximate to titanium powder size). Hence, the adjustment of the network structure size can be realized by controlling the particle size of the titanium powders [45].

Hot deformation characteristics

Stress–strain response

Compositing leads to a substantial improvement in the high-temperature tensile performance of Ti65 alloy, as depicted in Fig. S1 and detailed in Table S1. At 600 °C and 700 °C, the tensile strength of the TiBw/Ti65 composites increases by 17% and 16%, respectively, compared to the Ti65 alloy. To advance industrial applications, the next step involves evaluating its processing deformability through Gleeble 1500D testing. The high-temperature compression stress–strain curves of the TiBw/Ti65 composites at different strain rates under the same temperature are shown in Fig. 5a–d. It can be clearly seen that the flow behavior of composites is significantly impacted by the deformation temperature and strain rate to a large extent. The curves can be divided into three typical stages at high strain rates (1 s^{-1} and 0.1 s^{-1}): (1) Work hardening stage [46], (2) Flow softening stage [47], (3) Steady-state flow stage, as shown by the red and black curves in Fig. 5. However, with decreasing strain rates (0.01 s^{-1} and 0.001 s^{-1}), the stress–strain curves transform from a dynamic recrystallization type to a dynamic recovery type curve. The curves mainly exhibit the stages of work hardening and steady-state flow, as shown by the blue and green curves in Fig. 5. The flow stress reaches its peak value and remains nearly constant. This is because at lower strain rates, the deformation

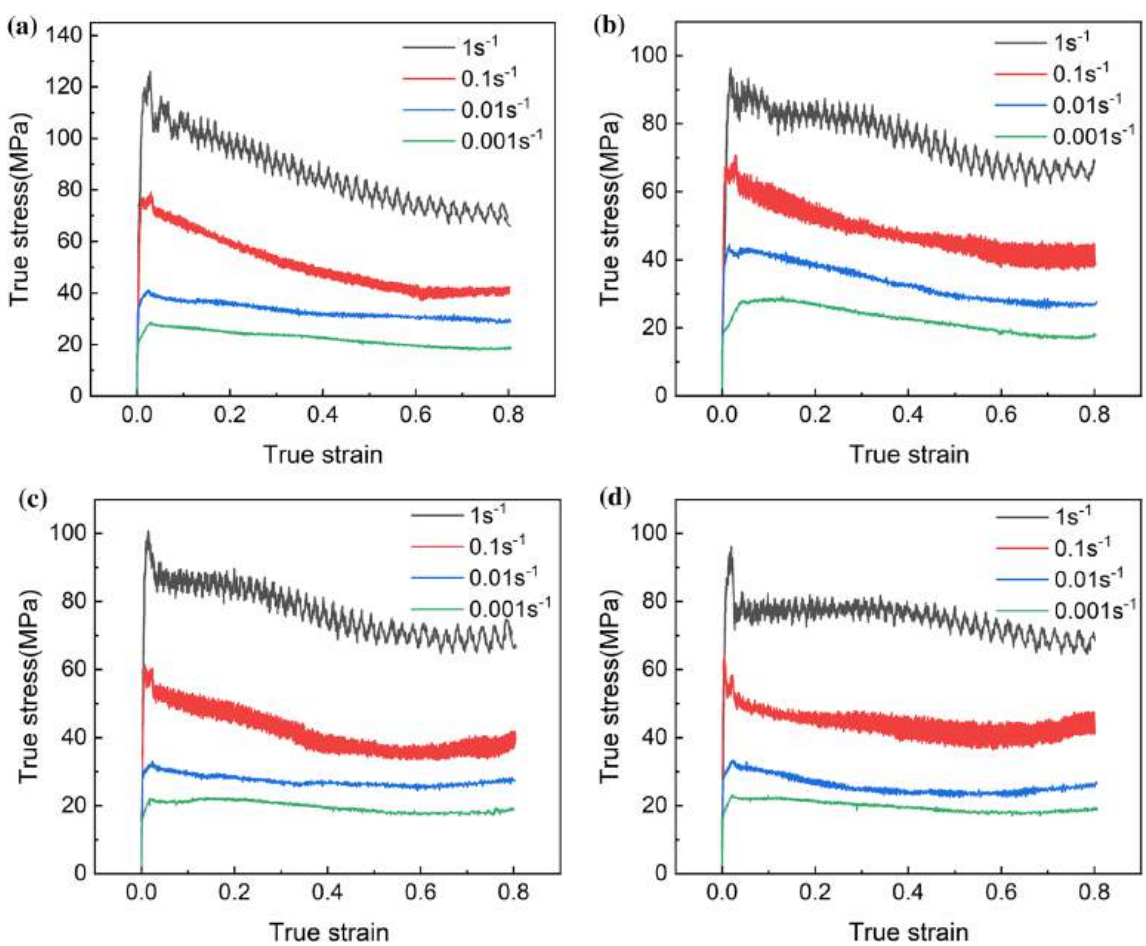

Figure 5 True stress–strain curves of the TiBw/Ti65 composites after hot compression under various strain rates: **a** 1040 °C; **b** 1060 °C; **c** 1080 °C; **d** 1100 °C.

duration is longer, and the high-density dislocations generated by work hardening are mutual annihilation through dynamic recovery, resulting in a dynamic equilibrium between work hardening and dynamic softening.

As can be seen in Fig. 5a, when the deformation temperature is fixed, increasing the strain rate from 0.001 to 1 s^{-1} results in a significant increase in flow stress and peak stress, indicating a high strain rate sensitivity of the composite. At a deformation temperature of 1040 °C, the peak stress of the composite reaches 126 MPa at a strain rate of 1 s^{-1}; while, it is 28 MPa at 0.001 s^{-1}, representing a 4.5-fold increase in flow stress. With higher strain rates, dislocation multiplication and motion speed are faster, leading to more pronounced work hardening effects caused by dislocation pile-ups, resulting in an increase in flow stress. It is noteworthy that when the strain rate is relatively high (1 s^{-1}, 0.1 s^{-1}), the true stress–strain curves exhibit oscillations, attributed to dynamic recrystallization and the fracture of TiB whiskers [36, 37]. Subsequent sections will characterize the recrystallization behavior.

Higher deformation temperature (from 1040 to 1100 °C) at a constant strain rate results in reduced peak stress in the composites. However, the flow stress at the steady-state flow stage remains almost the same. Although the deformation temperatures are both within the β single-phase region, there is still a certain temperature sensitivity. For example, at a strain rate of 0.1 s^{-1}, the peak stress at a deformation temperature of 1040 °C is 79 MPa (Fig. 5a); while, it is 62 MPa at 1100 °C (Fig. 5d). Moreover, as the strain rate decreases, the gap in peak stress gradually narrows. The deformation mechanisms will be further analyzed in the subsequent sections, integrating microscopic observations of the microstructure.

Kinetic analysis

The hot deformation behavior of alloys and metal matrix composites can be described using Arrhenius equation [48]. The relationship between flow stress (σ_p), strain rate ($\dot{\varepsilon}$) and deformation temperature (T) can be expressed by typical hyperbolic sine function, as shown in Eqs. (2) and (3):

$$\dot{\varepsilon} = AF\left(\sigma_p\right)\exp\left(-\frac{Q}{RT}\right) \tag{2}$$

$$F\left(\sigma_p\right) = \begin{cases} \sigma_p^{n_1} & \alpha\sigma < 0.8 \\ \exp\left(\beta\sigma_p\right) & \alpha\sigma > 1.2 \\ \left[\sinh\left(\alpha\sigma_p\right)\right]^n & \text{for all } \sigma \end{cases} \tag{3}$$

where Q is the apparent activation energy for hot deformation (kJ/mol), and R is the universal gas constant (8.314 J/mol K), A, n, n_1, α and β are material constants, and $\alpha = \beta/n_1$.

The constitutive equation for is expressed in three different forms, each applicable under different conditions. When operating at high temperatures and low stress levels ($\alpha\sigma < 0.8$), the deformation behavior of the material follows a power-law function. Under high stress levels ($\alpha\sigma > 1.2$), the deformation of the material is often described by an exponential function. In a wide range of stress levels, the deformation of the material can be represented by a hyperbolic sine function.

The peak stresses under different deformation conditions for the composite are shown in Table 1. The values of n_1 and β can be obtained by fitting the peak stress of the material under different deformation conditions into the equation mentioned above. For the deformation of network structure TiBw/Ti65 composites in the single-phase region, n_1 is determined to be 4.7356 and β is 0.0838 by applying linear regression [49]. Using these values, α can be calculated as 0.0177.

In addition, Eq. (2) can be transformed:

$$\ln[\sinh(\alpha\sigma)] = \frac{1}{n}\cdot\ln\dot{\varepsilon} + \frac{Q}{nR}\cdot\frac{1}{T} - \frac{\ln A}{n} \tag{4}$$

By taking $\ln[\sinh(\alpha\sigma)]$ as y, $\ln\dot{\varepsilon}$ as x_1, and $1/T$ as x_2, a linear regression in the form of $y = a + bx_1 + cx_2$ can be performed. Following the approach presented by Zhang et al. [49], by substituting the obtained α value into the corresponding Eq. (4). This regression

Table 1 Peak stress of TiBw/Ti65 composites under different deformation conditions (MPa)

Temperature (°C)	Strain rate			
	1 s^{-1}	0.1 s^{-1}	0.01 s^{-1}	0.001 s^{-1}
1040	126	79	41	28
1060	96	70	44	28
1080	100	61	31	22
1100	96	62	33	23

Table 2 Material constants of the present TMCs

Phase region	A	α (MPa^{-1})	n	Q (kJ mol^{-1})
β	7.00×10^{10}	0.0177	3.5572	321.57

analysis allows for the determination of other relevant material constants A, n, and Q, as shown in Table 2.

Substituting the obtained material constants into the hyperbolic sine Arrhenius equation, the fitted constitutive equation for hot deformation can be expressed as Eq. (5).

$$\dot{\varepsilon} = 7.00\times10^{10}\left[\sinh\left(0.0177\sigma_{\mathrm{p}}\right)\right]^{3.5572}\exp\left(-\frac{321570}{\mathrm{RT}}\right) \tag{5}$$

The definition of the Zener–Hollomon parameter [50, 51], which is a strain rate compensation factor in the constitutive equation for hot deformation of materials, is given by Eq. (6).

$$Z = \dot{\varepsilon}\exp\left(\frac{Q}{RT}\right) \tag{6}$$

Substituting the Zener–Hollomon parameter into the constitutive equation, and taking the logarithm of both sides, we obtain:

$$\ln Z = \ln A + n\ln[\sinh(\alpha\sigma)] \tag{7}$$

By substituting the activation energy for hot deformation into Eq. (6), we can determine the Z parameter for different deformation conditions. Then, using the Eq. (7) to perform a linear regression between ln(Z) and ln[sinh($\alpha\sigma$)], we can obtain a correlation coefficient R^2 of 0.9679. From Fig. 6, it can be observed that there is a good agreement between the linear relationship and the experimental data. This indicates that the hyperbolic sine relationship given by Eq. (5) can be used to describe the hot deformation behavior of the TiBw/Ti65 composites with a network architecture.

The obtained activation energy Q for the TiBw/Ti65 composites in the β phase region is 321.57 kJ/mol. It is noteworthy that this activation energy is much higher than the self-diffusion activation energy of β-Ti, which is 153 kJ/mol [52]. This indicates that the flow softening behavior of the material is predominantly controlled by dynamic recovery and dynamic recrystallization associated with dislocation

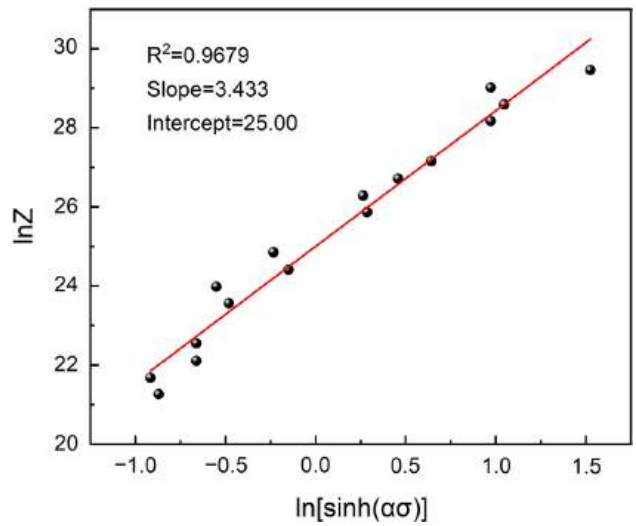

Figure 6 The relationship between the Z-parameter and flow stress.

slip. It is evident that the introduction of TiB whiskers effectively impedes dislocation motion. Ma et al. [53] found that the presence of TiC in TiC/Ti-1100 composites hinders grain boundary and dislocation motion, significantly increasing the thermal activation energy of high-temperature titanium-based composites, which is consistent with the findings of this study. Moreover, compared to the network-structured TiBw/TA15 composites [49], the TiBw/Ti65 composites exhibits a similar activation energy in the β phase region but significantly higher n value. This suggests that the hot deformation of TiBw/Ti65 composites is predominantly governed by dislocation creep driven by dislocation motion; while, the hot deformation of TiBw/TA15 composites in the single-phase region is more dominated by diffusion creep, which corresponds to the presence of a higher proportion of high-melting-point alloying elements in TiBw/Ti65 composites. The addition of tantalum, tungsten, and other elements effectively reduces the diffusion coefficient in the Ti65 matrix, allowing the dislocation mechanism to be sustained at higher temperatures and better maintaining the high-temperature strength of the material.

Processing maps

Based on the dynamic material model (DMM) perspective proposed by Prasad [54], the material processing process can be viewed as an energy

dissipation system. Furthermore, the total dissipation power P is composed of the dissipation quantity G and the dissipation co-quantity J. Here, J represents the energy consumed by structural changes; while, G represents the energy dissipated in the form of heat.

$$P = \sigma \cdot \dot{\varepsilon} = \int_0^{\dot{\varepsilon}} \sigma \mathrm{d}\dot{\varepsilon} + \int_0^{\sigma} \dot{\varepsilon} \mathrm{d}\sigma = G + J \tag{8}$$

The strain rate sensitivity factor m is defined as the ratio of the dissipation co-quantity (J) to the dissipation quantity (G) under a constant stress, as shown in Eq. (9):

$$m = \frac{\mathrm{d}J}{\mathrm{d}G} = \frac{\partial(\log \sigma)}{\partial(\log \hat{\varepsilon})} \tag{9}$$

When $m = 1$, the dissipation co-quantity J reaches its maximum value $J_{\max}$. In this case, the energy dissipation efficiency factor η can be obtained.

$$J = J_{\max} = \frac{\sigma \dot{\varepsilon}}{2} \tag{10}$$

$$\eta = \frac{J}{J_{\max}} = \frac{2m}{m+1} \tag{11}$$

According to the principle of maximum plastic strain deformation, the condition for rheological instability can be obtained as follows [55]:

$$\xi(\dot{\varepsilon}) = \frac{\partial \log\left(\frac{m}{m+1}\right)}{\partial \log \dot{\varepsilon}} + m < 0 \tag{12}$$

The calculation of the hot processing map in this study was based on the improved method proposed by Zhang et al. [49], which still utilizes Prasad's instability criterion. However, instead of calculating J using the strain rate sensitivity factor m, an integration method is employed directly for the calculation.

Based the aforementioned method, using the hot compression flow stress of the composites at $\varepsilon = 0.2$ and $\varepsilon = 0.4$, the hot processing maps for the composites were developed by combining the power dissipation and instability maps This was done to optimize the best deformation process for the TiBw/Ti65 composites, and the plotted hot processing maps are shown in Fig. 7.

From Fig. 7, it can be observed that the hot processing efficiency of the composites in the β single-phase region changes gradually. The composite exhibits higher hot dissipation efficiency at higher strain rates (1–0.1 s^{-1}); while, the region of deformation instability occurs at 1070–1100 °C and 0.001 s^{-1}, indicating that deformation instability occurs at high temperatures and low strain rates, which is mainly due to excessive grain growth. The peak of hot dissipation efficiency appears at 1070–1100 °C and 1–0.1 s^{-1}, corresponding to higher deformation temperatures and faster strain rates, and it is far away from the instability region. This indicates the presence of a hot processing scope

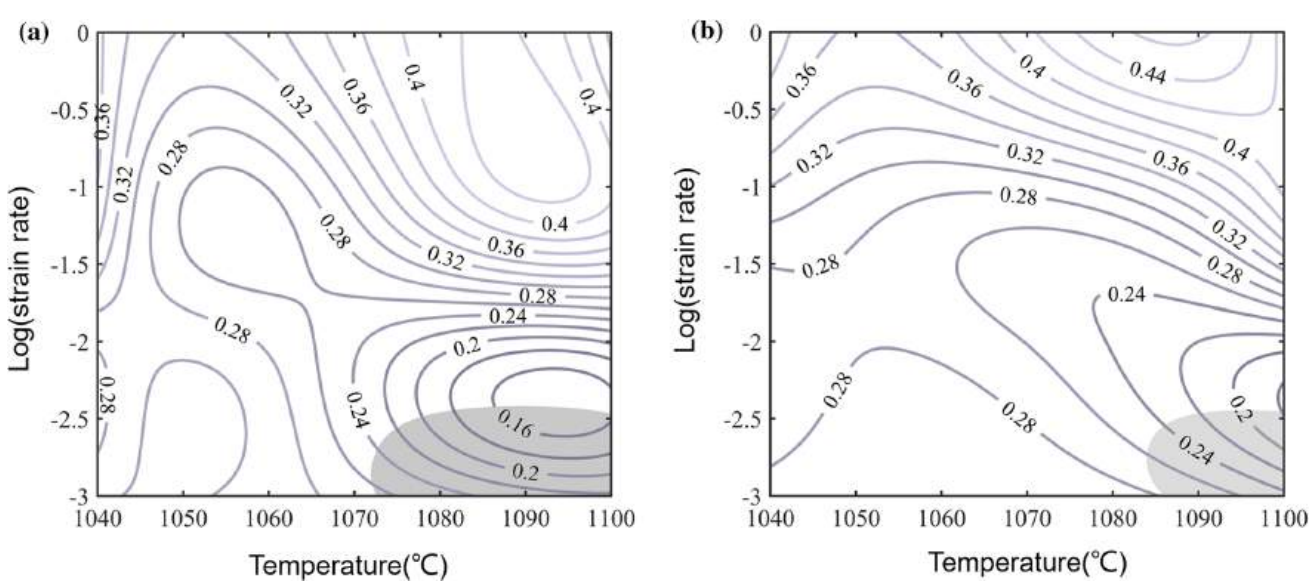

Figure 7 Processing maps of the TiBw/Ti65 composites under true strain of: **a** 0.2; **b** 0.4.

for the TiBw/Ti65 composites with a network architecture at that range of conditions. Noteworthy, previous research [23] has found that Ti65 alloy exhibits an instability region when the strain rate exceeds 0.01 s^{-1}. It can be concluded that the introduction of TiBw has altered the peak efficiency zone and the hot-working range of the composite, allowing for deformation methods such as rolling with high strain rates.

Microstructure evolution during hot compression deformation

During high-temperature compression, the deformation of the TiBw/Ti65 composites exhibited inhomogeneity, with variations in deformation, temperature, and microstructure at different locations. For the network structure composites, the deformation of each network structure in different locations can intuitively reflect the deformation in that region. Figure 8 illustrates the axial microstructural features of the network structure TiBw/Ti65 composites after deformation at 1040 °C/0.1 s^{-1}, which can be divided into four regions: Region I is the concentrated deformation zone, and the microstructure exhibits a fibrous distribution along the deformation direction, which is the main observation area in the subsequent microstructure evolution analysis. Region II is cold zone at both ends, and frictional forces exist between the sample and the anvils, resulting in minimal plastic deformation in this region. Region III is the shoulder tensile stress zone, located in the shoulder area of the hot-compressed sample. Region IV is the edge bulging zone, primarily serving to accommodate deformation.

After hot compression deformation of the composite, the microstructural characteristics of different regions show significant differences, as shown in Fig. 8b–e, primarily due to temperature variations in different regions. Regions II and III contact with the water-cooled anvils, where the actual temperature is lower than the β phase transformation temperature. After quenching, a substantial amount of lamellar residual α_p can be observed, as shown in Fig. 8c, d. On the other hand, Regions I and IV reach the deformation temperature, with Region I experiencing the most

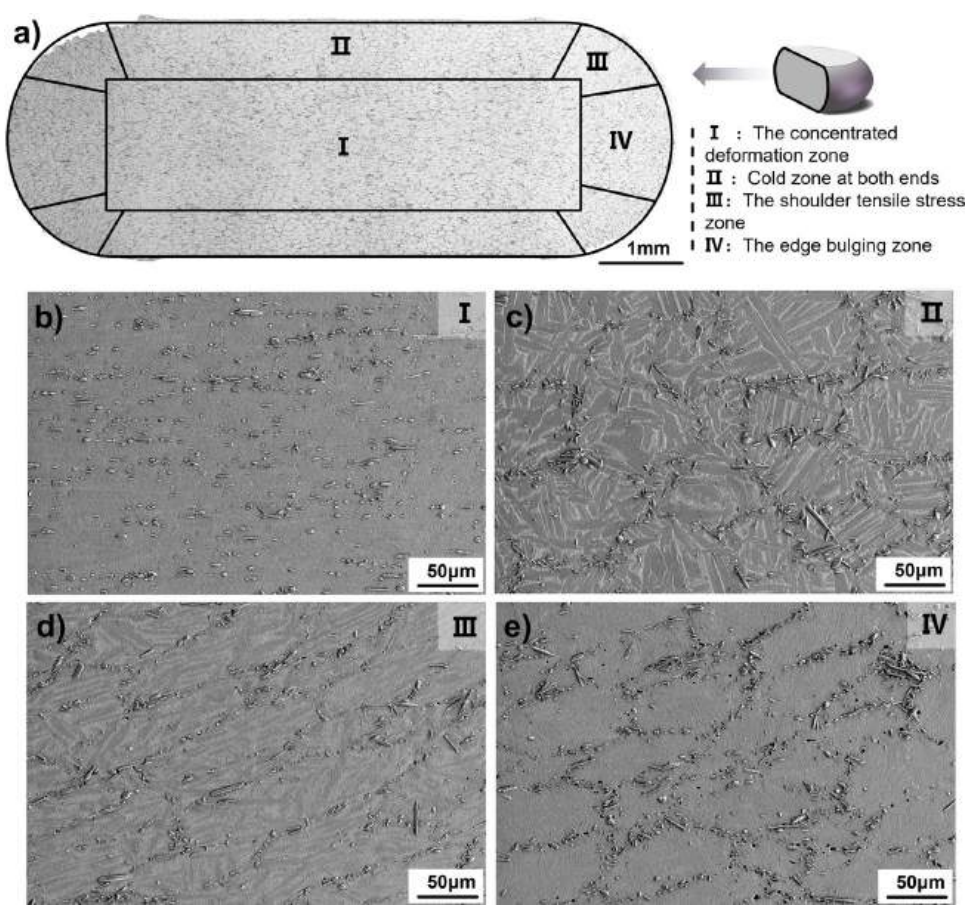

Figure 8 Metallographic photograph of the cross section of TiBw/Ti65 composites under high-temperature compression: **a** Metallographic photograph; **b–e** Metallographic photographs of regions I, II, III and IV in the cross section of the composite, respectively.

intense deformation as it is closer to the central part. The large amount of heat generated during deformation in Region I is not easily dissipated, potentially leading to a more complete phase transformation in this region. Therefore, Regions I and IV exhibit a significant amount of fine martensite, and the microstructure is defined as β_T microstructure since it is entirely transformed by rapid cooling of β-Ti at high temperature. In fact, the microstructures characteristics after hot compression are similar under different deformation conditions, with the difference being a slight difference in the percentage of each region.

In order to investigate the microstructure evolution in the peak efficiency region of the processing map, the microstructure of the specimen deformed at 1100 °C/1 s^{-1} is characterized. The EBSD result is shown in Fig. 9. The matrix microstructure is composed of a large amount of fine secondary α phases without primary α phase, as shown in Fig. 9a, which is due to the deformation temperature is higher than the β transition temperature. On the one hand, at high strain rates, the sample have insufficient time for dynamic recovery and growth of dynamically recrystallized grains. On the other hand, the introduction of TiB whiskers can obstruct dislocation motion due to its ceramic nature [56], generate distortion energy, and provide driving force for dynamic recrystallization. Thus, significant dynamic recrystallization occurs in the composite at high temperatures and high strain rates, forming fine secondary a-phases. The above phenomenon validates the adequately dynamic recrystallization, which

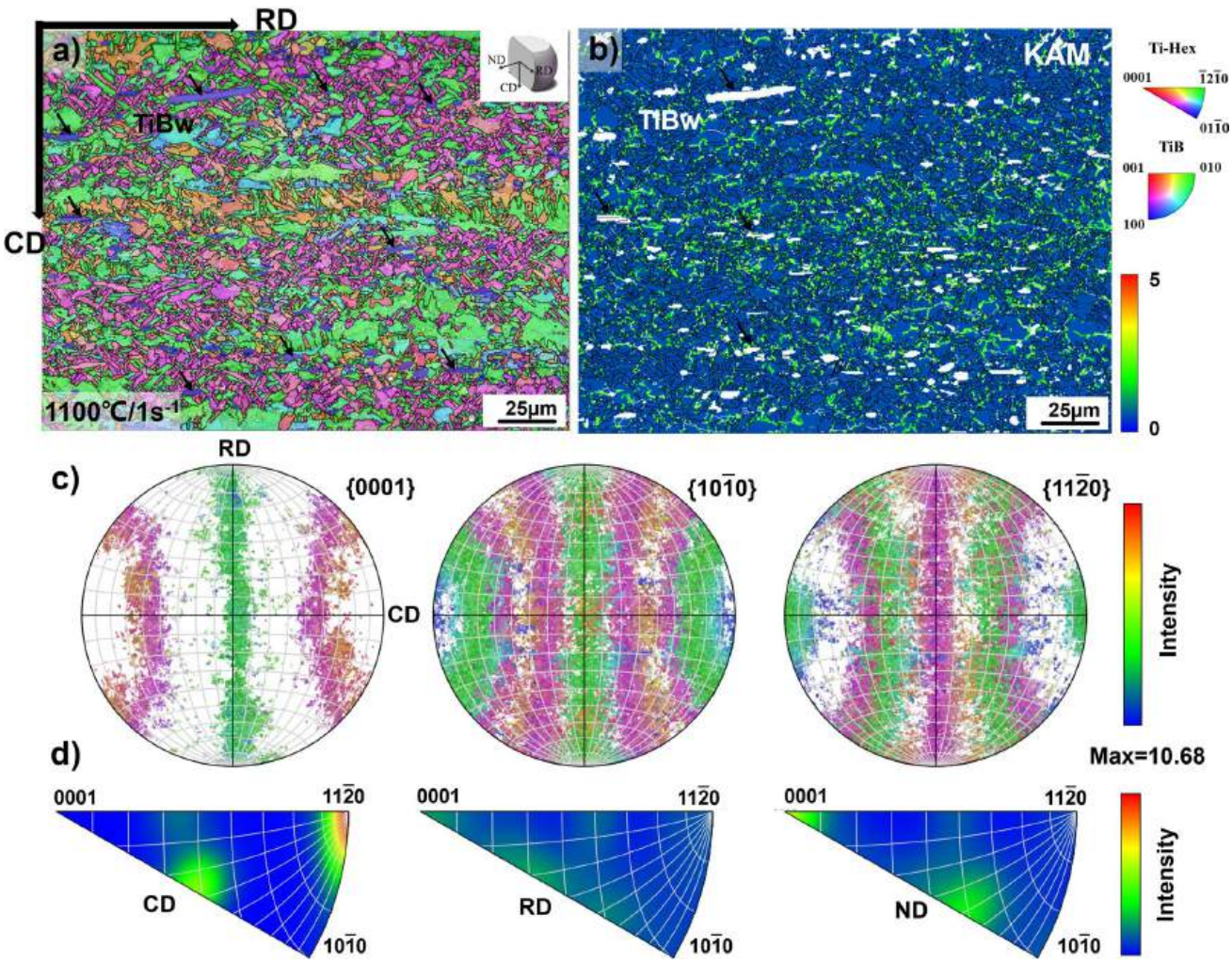

Figure 9 EBSD characterization results of specimens deformed at 1100 °C/1 s^{-1}: **a** the IPF map; **b** the KAM map; **c**, **d** the pole figure and inverse pole figure of α phase calculated with orientational information in **a**, respectively.

corresponds to the peak efficiency region in hot processing (Fig. 7). In general, dynamic recrystallization is beneficial for hot processing of the composite, which not only reduces the deformation resistance of the material, but also regulate its microstructure, leading to desirable processability and improved mechanical properties.

Figure 9b shows the Kernel Average Misorientation (KAM) maps of the hot compressed microstructures at 1100 °C/1 s^{-1}. The KAM value represents the average misorientation difference between a scanning point and its neighboring data points, and it can be used to describe the distribution of geometrically necessary dislocations (GNDs). Li et al. [39] analyzed the degree of grain deformation and the dynamic recrystallization mechanism in TiB/TA15 composites using KAM maps of dislocation distribution. In this study, the KAM maps are used to analyze the dynamic recrystallization mechanism of grains during the hot compression process. A higher KAM value indicates a higher degree of deformation and a higher dislocation density. In Fig. 9b, it can be observed that regions with higher KAM values are mainly distributed at the interface between TiBw and the matrix, as well as within elongated grains. The regions with high KAM values within grains indicate that these deformed grains have accumulated a large number of dislocations and strains, providing driving force for dynamic recrystallization. TiBw hinder the motion of dislocations during the hot compression process. When a certain level of dislocation accumulation occurs near TiBw, it can promote the generation of recrystallized grains. The large number of accumulated dislocations within grains formed substructures through dislocation entanglement, as shown in Fig. 9b, which then transformed into low-angle grain boundaries or even high-angle grain boundaries, leading to continuous dynamic recrystallization (CDRX) [57]. Moreover, as shown in Fig. 9a, the serrated HAGBs (High-Angle Grain Boundaries) acted as potential nucleation sites for dynamic recrystallization, and the interface between TiBw and the matrix was prone to undergo dynamic recrystallization, resulting in a "necklace-like" microstructure. This phenomenon is commonly observed in discontinuous dynamic recrystallization (DDRX) mechanism. Therefore, it is believed that the hot compression deformation process mainly involves CDRX and DDRX as the two dynamic recrystallization mechanisms. As a result, the hot compression process of TiBw/Ti65 composites is mainly controlled by dislocation movement, and there are two dynamic recrystallization mechanisms (DDRX and CDRX).

The TiBw at the network interface effectively limit the growth of the prior β grains during the hot compression process, which makes the hot compression microstructure show a lamellar character. And a significant preference orientation in the hot deformation microstructure can be observed from Fig. 9a. Furthermore, Fig. 9c shows the pole figure (PF) of the microstructure of the composite after deformation at 1100 °C/1 s^{-1}. It can be found that it exhibits an obvious fiber texture characteristic. By calculating its inverse pole figure (IPF), as shown in Fig. 9d, the microstructure after deformation has a strong $< \bar{1}2\bar{1}0 >$//CD fiber texture and $< 01\bar{1}1 >$//CD fiber texture.

Since the deformation temperature is in the β single-phase region, the HCP structure of α-Ti is transformed into the BCC structure of β-Ti during heating. Only β-Ti undergoes hot compression deformation, and the microstructure retained after quenching is transformed from high temperature β-Ti. Therefore, in order to reveal the reasons for the generation of texture after hot deformation of composite, it is necessary to investigate the microstructure characteristics of the high-temperature β-phase after hot deformation. For the sintered composites, the α phases transformed from the same β grain satisfy the famous BOR, that is, $\{110\}_\beta//\{0001\}_\alpha$, and $< 111 >_\beta//< 11\bar{2}0 >_\alpha$. When the material is cooled, the Burgers relationship between the α/β phases makes the misorientation between the α phases transformed in the same β grain concentrated at: 10°, 60°, 63°, 90° [38]. In order to investigate the recrystallization and texture characteristics of the composite, the prior β grains were reconstructed based on the BOR, as shown in Fig. 10a. The black line in the figure shows the reconstructed β grain boundaries. It can be observed that the β grains are striped at high temperatures, attributed to the limiting effect of TiBw on grain growth. On the one hand, one network unit corresponds to one prior β grain before deformation, and multiple prior β grains appear after deformation, and on the other hand, fine recrystallized grains are also present at the edge of grain boundaries and at the TiBw. All these phenomena intuitively indicate that the composite deformation is dominated by dynamic recrystallization under this condition.

The hot deformation of β-Ti at high temperatures produces a strong $< 001 >$//CD and weak $< 111 >$//CD texture, as shown in Fig. 10b, which attributes to the orientation transformation and dynamic

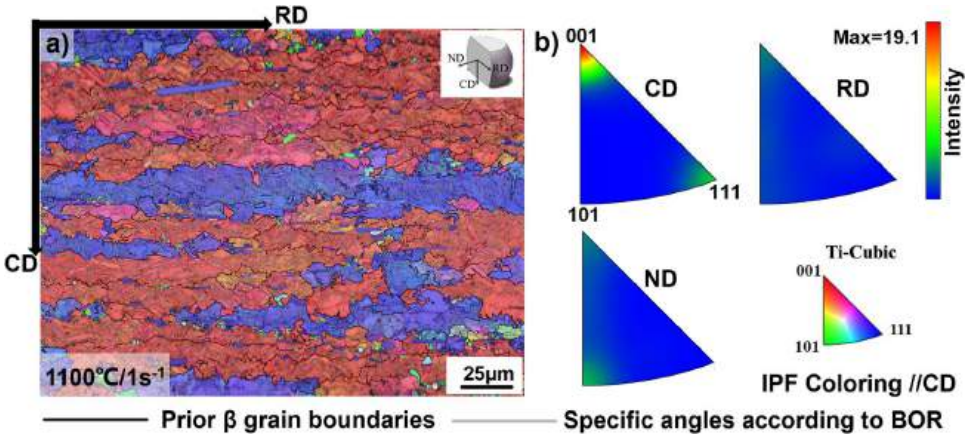

Figure 10 EBSD dates of the reconstructed β phase deformed at 1100 °C/1s^{-1}: **a** the IPF color map; **b** the inverse pole figure of the reconstructed β calculated with orientational information in **a**.

recrystallization during hot compression. The phase transition occurs during quenching, based on the BOR, leading to the $< \bar{1}2\bar{1}0 >$//CD fiber texture and $< 01\bar{1}1 >$ //CD fiber texture of α phase [58, 59].

Figure 11 shows the inverse pole figure of TiBw after hot compression, and it can be seen that TiBw has strong [100]//CD texture, and weak [010]//RD and [010]//ND texture, which is generated by the compression deformation that makes the TiBw oriented alignment. Combined with the fact that the TiB phase is an orthorhombic crystal system with the fastest growth rate along [010], i.e., the whisker's long-axis direction is distributed along the radial (RD/ND) alignment, and the slowest growth along [100], i.e., the whisker's flattened surface normal phase is parallel to the compression direction (CD), It is worth mentioning that, this distribution characteristic of TiBw has been demonstrated in various investigations [49, 59, 60].

Texture identification

Figure 12 shows the pole figures (PF) of the ND plane in the microstructure of the network matrix under different deformation conditions. It can be found that the composites under different deformation conditions exhibit the similar fiber texture due to the introduction of TiBw at the network interface, which limits the growth of β grains at high temperatures. However, the pole density varies significantly in some regions of the pole figure. No high-density poles are seen on the pole figure of {0001} plane of the deformation microstructure at 1040 °C/1 s^{-1}, as shown in Fig. 12a, and as the strain rate decreases, two symmetrically distributed high-density poles appear on the pole figure of {0001} plane of the deformation microstructure at 1040 °C/0.001 s^{-1}, as shown in Fig. 12c. In addition, the texture strength increases from 9.52 Multiples of

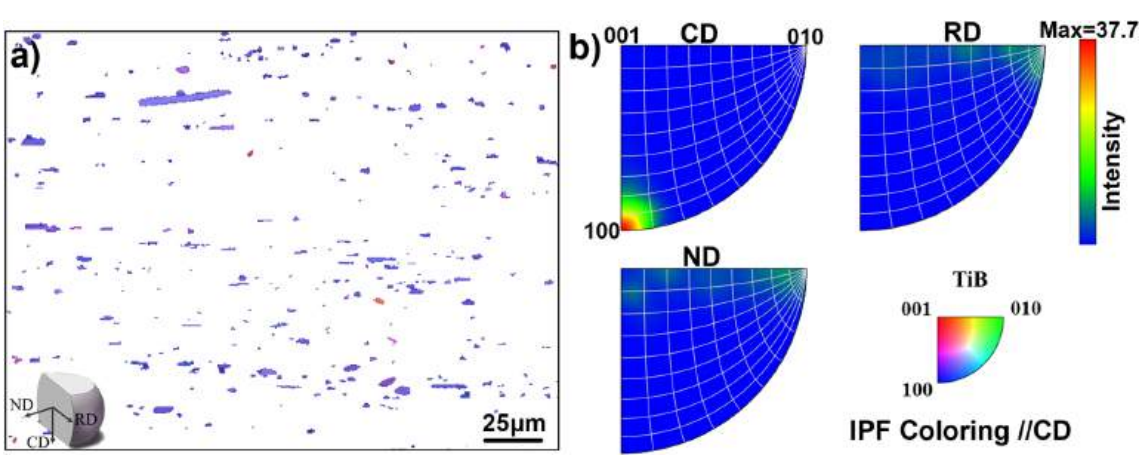

Figure 11 EBSD characterization results of specimens deformed at 1100 °C/1 s^{-1}: **a** the IPF map of TiBw; **b** the inverse pole figure of TiBw calculated with orientational information in **a**.

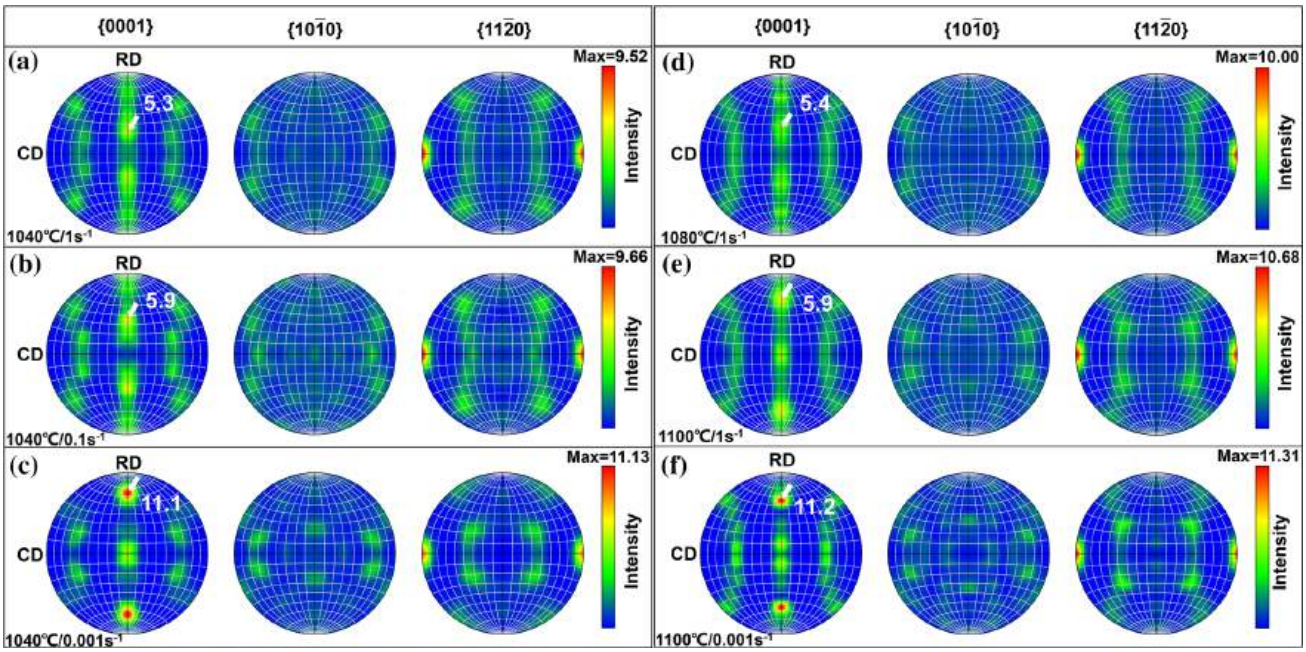

Figure 12 Pole figure of α phase in different deformation conditions: **a** 1040 °C/1 s^{-1}; **b** 1040 °C/0.1 s^{-1}; **c** 1040 °C/0.001 s^{-1}; **d** 1080 °C/1 s^{-1}; **e** 1100 °C/1 s^{-1}; **f** 1100 °C/0.001 s^{-1}.

uniform density (Mud) to 11.13 Mud as the strain rate decreases, as depicted in Fig. 12a–c. At the same time, as the deformation temperature increases, a higher density of poles also can be observed on the pole figure of {0001} plane in both Fig. 12d, e. The texture strength increases from 9.52 to 10.68Mud as deformation temperature increases. It can be observed from comparing Fig. 12a–e that the effect of the deformation temperature on the high-density poles on the pole figure of {0001} plane is smaller than the effect of the strain rate. In addition, the highest strength of the texture is found at the highest deformation temperature and the lowest strain rate (1100 °C/0.001 s^{-1}), and two symmetrically distributed high-density poles are also present on the pole figure of {0001} plane.

To investigate the influence of deformation conditions on the texture of microstructures of the TiBw/Ti65 composites, recrystallized grains and deformed grains were extracted under the deformation condition of 1100 °C/0.001 s^{-1}, as shown in Fig. 13a, c. The pole figure was divided by Aztec Crystal software, the hot compression texture can be divided into recrystallized texture and thermally deformed texture, as shown in Fig. 13b, d respectively. The pole density on the {0001} plane in the pole figure of fine recrystallized grains is low. Distinct fiber texture characteristics are presented by the recrystallized grains. A high density of poles is observed on the {0001} planes, exhibiting a symmetric distribution. This is mainly due to the following reasons: (1) At low temperature and high strain rate, a higher fraction of recrystallized grains is present, and the crystallographic orientation difference between recrystallized grains and the parent phase is significant. As a result, the pole points in the pole figure of recrystallized grains are more scattered, and the texture strength is relatively low. (2) With increasing deformation temperature and decreasing strain rate, the fraction of recrystallized grains significantly decreases, and the deformed grains have sufficient time to grow at high temperature. This leads to the presence of high-density pole points in the pole figure of deformed grains.

The texture is affected by deformed grains and recrystallized grains. Under different deformation conditions, varying degrees of recrystallization result in differences in corresponding texture characteristics. It also indicates that the degree of recrystallization decreases with increasing temperature and decreasing strain rate. Furthermore, analyzing the distribution of pole density in the pole figures provides a novel method for characterizing microstructural features under different deformation conditions.

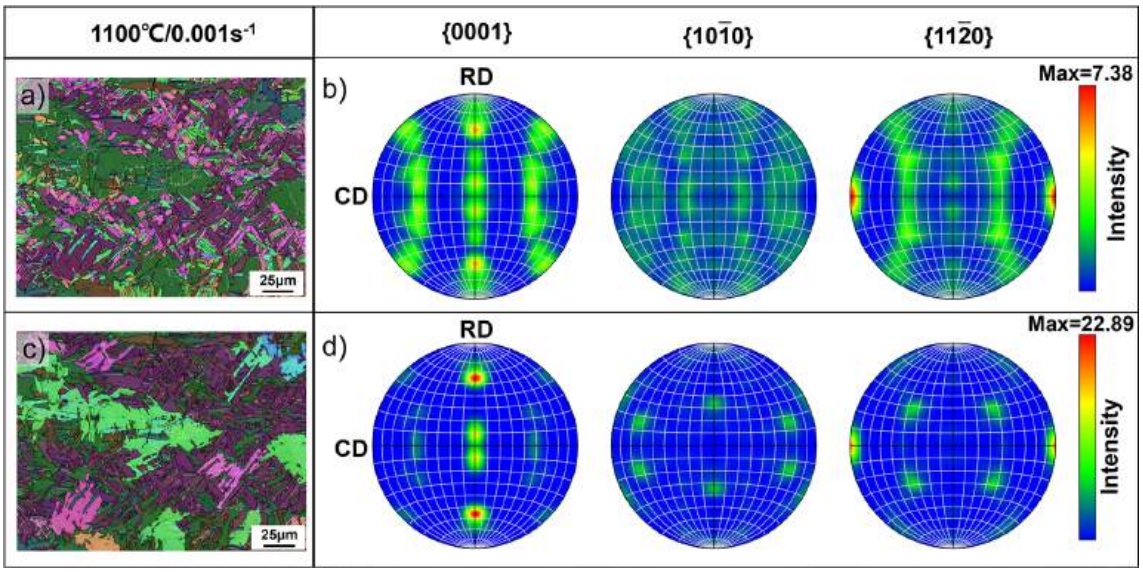

Figure 13 EBSD characterization results of specimens deformed at 1100 °C/0.001 s^{-1}: **a**, **c** the IPF color map of recrystallized grains and deformation grains, respectively; **b**, **d** the pole figure of α phase calculated with orientational information in **a**, **d**, respectively.

Conclusions

In the present work, the hot compression tests were conducted on a network architecture TiBw/Ti65 composites in the β single-phase region under different deformation conditions. The deformation behavior and the microstructural features of the composite at different deformation conditions were characterized. The main conclusions were drawn as follows:

1. A network architecture TiBw/Ti65 composites were successfully prepared through low-energy ball milling and hot-press sintering techniques. The composite matrix consists of lamellar α phase and intergranular β phase. TiB whiskers are discontinuously distributed at the network boundaries, effectively restraining the growth of the β phase at high temperature.
2. The TiBw/Ti65 composites show a high sensitivity to strain rate and temperature. The composites exhibit dynamic recrystallization as the dominant mechanism at high strain rate (1–0.1 s^{-1}). And the microstructural analysis reveals the presence of two dynamic recrystallization mechanisms: continuous dynamic recrystallization and discontinuous dynamic recrystallization. At low strain rate (0.01–0.001 s^{-1}), dynamic recovery becomes the predominant mechanism.
3. Constitutive equations and hot processing maps are obtained through flow stress calculations. The activation energy for hot deformation in the β single-phase region is determined to be 321.57 kJ/mol. And the suitable hot processing parameters for the composite are found to be in the range of 1070–1100 °C at strain rates of 1–0.1 s^{-1}.
4. After hot compression deformation, the texture of the specimens deformed in β region featured a strong $<\bar{1}2\bar{1}0>$//CD fiber texture and $<01\bar{1}1>$ //CD fiber texture, which was inherited from the high temperature β grains. Besides, TiBw reinforcements show a pronounced [100]//CD texture and a weak [010]//RD and [010]//ND texture.

Acknowledgements

This work is financially supported by National Key R&D Program of China [No. 2022YFB3707405], the National Natural Science Foundation of China [NSFC, Grant Nos. 52261135543, U22A20113, 52171137], Heilongjiang Touyan Team Program, Heilongjiang Provincial Natural Science Foundation of China [Grant No. TD2020E001], and Joint Guidance Foundation of the Natural Science Foundation of Heilongjiang Province of China [No. LH2023E031].

Author contributions

SX contributed to investigation, data curation, formal analysis, writing—original draft, writing—review and editing. QA contributed to conceptualization and project administration. SW contributed to conceptualization, writing—review and editing. RZ contributed to methodology and visualization. XC contributed to investigation. RC contributed to visualization. LH contributed to supervision, resources, and funding acquisition. SZ contributed to writing—review and editing. LG contributed to supervision.

Data and code availability

Data will be made available on request.

Declarations

Conflict of interest The authors declare that they have no known competing financial interests or personal relationships that could have appeared to influence the work reported in this paper.

Ethical approval Neither people nor animals were used as subjects in this investigation.

Supplementary Information The online version contains supplementary material available at https://doi.org/10.1007/s10853-024-09461-3.

References

[1] Williams JC, Starke EA Jr (2003) Progress in structural materials for aerospace systems. Acta Mater 51(19):5775–5799

[2] Banerjee D, Williams J (2013) Perspectives on titanium science and technology. Acta Mater 61(3):844–879

[3] Peters M, Kumpfert J, Ward CH, Leyens C (2003) Titanium alloys for aerospace applications. Adv Eng Mater 5(6):419–427. https://doi.org/10.1002/adem.200310095

[4] Lu K (2010) The future of metals. Science 328(5976):319–320

[5] Chandravanshi VK, Bhattacharjee A, Kamat SV, Nandy TK (2014) Influence of thermomechanical processing and heat treatment on microstructure, tensile properties and fracture toughness of Ti-1100-0.1B alloy. J Alloys Compd 589:336–345. https://doi.org/10.1016/j.jallcom.2013.11.014

[6] Pototzky P, Maier H, Christ H-J (1998) Thermomechanical fatigue behavior of the high-temperature titanium alloy IMI 834. Metall Mater Trans A 29:2995–3004

[7] Tetyukhin V, Levin I, Ilyenko V, Bilibina E, Usova T, Padykova N (1995) Heat-resistant titanium alloys with enhanced heat resistance, thermal stability. Titanium 95(3):2430–2437

[8] Peng W, Zeng W, Wang Q, Yu H (2013) Characterization of high-temperature deformation behavior of as-cast Ti60 titanium alloy using processing map. Mater Sci Eng A 571:116–122. https://doi.org/10.1016/j.msea.2013.01.008

[9] Yue K, Liu J, Zhang H et al (2020) Precipitates and alloying elements distribution in near α titanium alloy Ti65. J Mater Sci Technol 36:91–96. https://doi.org/10.1016/j.jmst.2019.03.018

[10] Zhu Y, Wu X (2023) Heterostructured materials. Prog Mater Sci. https://doi.org/10.1016/j.pmatsci.2022.101019

[11] Gorsse S, Miracle DB (2003) Mechanical properties of Ti-6Al-4V/TiB composites with randomly oriented and aligned TiB reinforcements. Acta Mater 51(9):2427–2442. https://doi.org/10.1016/s1359-6454(02)00510-4

[12] Tjong SC, Mai Y-W (2008) Processing–structure–property aspects of particulate- and whisker-reinforced titanium matrix composites. Compos Sci Technol 68(3–4):583–601

[13] Jiao Y, Huang LJ, Wei SL, Peng HX, An Q, Jiang S, Geng L (2019) Constructing two-scale network microstructure with nano-Ti_5Si_3 for superhigh creep resistance. J Mater Sci Technol 35(8):1532–1542. https://doi.org/10.1016/j.jmst.2019.04.001

[14] Ma Z, Wang S, Huang L et al (2023) Synergistically enhanced strength and ductility of TiB/(TA15-Si) composites: a two-step HIP strategy. Compos Part B. https://doi.org/10.1016/j.compositesb.2023.110583

[15] Wang S, Huang L, An Q et al (2019) Regulating crack propagation in laminated metal matrix composites through architectural control. Compos Part B. https://doi.org/10.1016/j.compositesb.2019.107503

[16] Chen R, An Q, Wang S et al (2022) Overcoming the strength-ductility trade-off dilemma in TiBw/TC18 composites via network architecture with trace reinforcement. Mater Sci Eng A. https://doi.org/10.1016/j.msea.2022.143092

[17] Huang L, An Q, Geng L et al (2021) Multiscale architecture and superior high-temperature performance of discontinuously reinforced titanium matrix composites. Adv Mater 33(6):e2000688. https://doi.org/10.1002/adma.202000688

[18] Huang LJ, Geng L, Peng HX (2015) Microstructurally inhomogeneous composites: Is a homogeneous reinforcement distribution optimal? Prog Mater Sci 71:93–168. https://doi.org/10.1016/j.pmatsci.2015.01.002

[19] Chen X, An Q, Jiang S, Jiao Y, Huang L, Geng L (2021) Revealing anti-oxidation mechanisms of titanium composite materials by detailed characterization of scale phase constitutions. Corros Sci. https://doi.org/10.1016/j.corsci.2021.109845

[20] An Q, Huang L, Qian Q et al (2022) Insights into in-situ TiB/dual-phase Ti alloy interface and its high load-bearing capacity. J Mater Sci Technol 119:156–166. https://doi.org/10.1016/j.jmst.2021.12.035

[21] Li M, Shi Z-Z, Wang Q, Cheng Y, Wang L-N (2023) Zn–0.8Mn alloy for degradable structural applications: hot compression behaviors, four dynamic recrystallization mechanisms, and better elevated-temperature strength. J Mater Sci Technol 137:159–175. https://doi.org/10.1016/j.jmst.2022.08.002

[22] Evans R, Hull R, Wilshire B (1996) The effects of alpha-case formation on the creep fracture properties of the high-temperature titanium alloy IMI834. J Mater Process Technol 56(1–4):492–501

[23] Zhang Z, Fan J, Tang B, Kou H, Wang J, Chen Z, Li J (2020) Microstructure/texture evolution maps to optimize hot deformation process of near-α titanium alloy. Prog Nat Sci 30(1):86–93. https://doi.org/10.1016/j.pnsc.2020.01.004

[24] Zhang Z, Fan J, Tang B et al (2020) Microstructural evolution and FCC twinning behavior during hot deformation of high temperature titanium alloy Ti65. J Mater Sci Technol 49:56–69. https://doi.org/10.1016/j.jmst.2020.02.026

[25] Zhang ZX, Fan JK, Wu ZH et al (2020) Precipitation behavior and strengthening–toughening mechanism of hot rolled sheet of Ti65 titanium alloy during aging process. J Alloys Compd. https://doi.org/10.1016/j.jallcom.2020.154786

[26] He B, Sun J, Ren Y, Li C, Yang G, Li X, Ni J (2022) Effect of heat treatment on microstructure and mechanical properties of laser-deposited Ti65 near-alpha titanium alloy. J Mater Res 37(8):1464–1474. https://doi.org/10.1557/s43578-022-00547-9

[27] Zhao D, Fan J, Zhang Z et al (2020) Microstructure and texture variations in high temperature titanium alloy Ti65 sheets with different rolling modes and heat treatments. Materials. https://doi.org/10.3390/ma13112466

[28] Zhang Z, Fan J, Li R et al (2021) Orientation dependent behavior of tensile-creep deformation of hot rolled Ti65 titanium alloy sheet. J Mater Sci Technol 75:265–275. https://doi.org/10.1016/j.jmst.2020.10.021

[29] Wang S, An Q, Zhang R et al (2022) Microstructure characteristics and enhanced properties of network-structured TiB/(TA15-Si) composites via rolling deformation at different temperatures. Mater Sci Eng A. https://doi.org/10.1016/j.msea.2021.142176

[30] Wang S, Huang L, Zhang R, An Q, Sun F, Meng F, Geng L (2022) Effects of rolling deformation on microstructure orientations and tensile properties of TiB/(TA15-Si) composites. Mater Charact. https://doi.org/10.1016/j.matchar.2022.112425

[31] Wan Q, Zhang B, Zhang F, Shang C, Xiong Y (2022) Interface-reaction reduction and hot rolling deformation of network structured graphene-TiB whiskers/Ti6Al4V composites by spark plasma sintering. J Mater Sci 57(44):20601–20614. https://doi.org/10.1007/s10853-022-07936-9

[32] Wang B, Huang LJ, Hu HT, Liu BX, Geng L (2015) Superior tensile strength and microstructure evolution of TiB whisker reinforced Ti60 composites with network architecture after β extrusion. Mater Charact 103:140–149. https://doi.org/10.1016/j.matchar.2015.03.029

[33] Wang B, Zhang H, Huang L, He J, Zhang Y, Wang W (2018) Evolution of microstructure and high temperature tensile properties of as-extruded TiBw reinforced near-α titanium matrix composite subjected to heat treatments. Sci China Technol Sci 61(9):1340–1345. https://doi.org/10.1007/s11431-018-9323-3

[34] Zhang R, Wang D, Yuan S (2017) Effect of multi-directional forging on the microstructure and mechanical properties of TiBw/TA15 composite with network architecture. Mater Des 134:250–258. https://doi.org/10.1016/j.matdes.2017.08.055

[35] Ozerov M, Klimova M, Sokolovsky V, Stepanov N, Popov A, Boldin M, Zherebtsov S (2019) Evolution of microstructure and mechanical properties of Ti/TiB metal-matrix composite during isothermal multiaxial forging. J Alloys Compd 770:840–848. https://doi.org/10.1016/j.jallcom.2018.08.215

[36] Wang B, Huang LJ, Geng L, Rong XD (2015) Compressive behaviors and mechanisms of TiB whiskers reinforced high temperature Ti60 alloy matrix composites. Mater Sci Eng A 648:443–451. https://doi.org/10.1016/j.msea.2015.09.026

[37] Wang B, Huang LJ, Liu BX, Geng L, Hu HT (2015) Effects of deformation conditions on the microstructure and substructure evolution of TiBw/Ti60 composite with network structure. Mater Sci Eng A 627:316–325. https://doi.org/10.1016/j.msea.2015.01.012

[38] Zhang HB, Wang B, Zhang YT, Li Y, He JL, Zhang YF (2020) Microstructure evolution and deformation

mechanisms of β phase in TiBw/Ti60 composites studied by reconstructing grain during the hot deformation. J Alloys Compd. https://doi.org/10.1016/j.jallcom.2020.153872

[39] Li Z, Kang Q, Wang G, Sui X, Liu Y, Luo S (2022) Microstructure evolution during hot-packed rolling and mechanical properties anisotropy of as-rolled network-structured TiBw/TA15 composites. Mater Sci Eng A. https://doi.org/10.1016/j.msea.2022.143518

[40] Zhang CJ, Sun YG, Chen YF et al (2019) Deformation behavior and microstructure evolution mechanism of 5vol.% (TiBw + TiCp)/Ti composites during isothermal compression. Mater Charact 154:212–221. https://doi.org/10.1016/j.matchar.2019.06.002

[41] Wang S, Huang L, Jiang S, Zhang R, An Q, Sun Y, Geng L (2020) Microstructure evolution and improved properties of laminated titanium matrix composites with gradient equiaxed grains. Sci China Technol Sci 63(12):2687–2697. https://doi.org/10.1007/s11431-020-1619-7

[42] Sen I, Tamirisakandala S, Miracle D, Ramamurty U (2007) Microstructural effects on the mechanical behavior of B-modified Ti–6Al–4V alloys. Acta Mater 55(15):4983–4993. https://doi.org/10.1016/j.actamat.2007.05.009

[43] Singh G, Ramamurty U (2021) Reprint: Boron modified titanium alloys. Prog Mater Sci. https://doi.org/10.1016/j.pmatsci.2021.100815

[44] Yang YF, Yan M, Luo S, Schaffer G, Qian M (2013) Modification of the α-Ti laths to near equiaxed α-Ti grains in as-sintered titanium and titanium alloys by a small addition of boron. J Alloys Compd 579:553–557

[45] Wei S, Huang L, Li X, Jiao Y, Ren W, Geng L (2019) Network-strengthened Ti-6Al-4V/(TiC+TiB) composites: powder metallurgy processing and enhanced tensile properties at elevated temperatures. Metall Mater Trans A 50(8):3629–3645. https://doi.org/10.1007/s11661-019-05244-7

[46] Cai D, Xiong L, Liu W, Sun G, Yao M (2007) Development of processing maps for a Ni-based superalloy. Mater Charact 58(10):941–946. https://doi.org/10.1016/j.matchar.2006.09.004

[47] Yan J, Pan QL, Li B, Huang ZQ, Liu ZM, Yin ZM (2015) Research on the hot deformation behavior of Al–6.2Zn–0.70Mg–0.3Mn–0.17Zr alloy using processing map. J Alloys Compd 632:549–557. https://doi.org/10.1016/j.jallcom.2015.01.228

[48] Mirzadeh H, Cabrera JM, Najafizadeh A (2011) Constitutive relationships for hot deformation of austenite. Acta Mater 59(16):6441–6448. https://doi.org/10.1016/j.actamat.2011.07.008

[49] Zhang R, Huang L, An Q, Geng L, Wang B, Jiao Y (2019) The hyperbolic constitutive equations and modified dynamic material model of TiBw/Ti-6.5Al-2.5Zr-1Mo-1V-0.5Si composites. Mater Sci Eng A. https://doi.org/10.1016/j.msea.2019.138329

[50] Sakai T, Jonas JJ (1984) Overview no. 35 dynamic recrystallization: mechanical and microstructural considerations. Acta Metall 32(2):189–209

[51] Sakai T, Belyakov A, Kaibyshev R, Miura H, Jonas JJ (2014) Dynamic and post-dynamic recrystallization under hot, cold and severe plastic deformation conditions. Prog Mater Sci 60:130–207

[52] Weiss I, Semiatin S (1998) Thermomechanical processing of beta titanium alloys—an overview. Mater Sci Eng A 243(1–2):46–65

[53] Ma F, Lu W, Qin J, Zhang D (2006) Hot deformation behavior of in situ synthesized Ti-1100 composite reinforced with 5 vol.% TiC particles. Mater Lett 60(3):400–405

[54] Prasad Y, Gegel H, Doraivelu S, Malas J, Morgan J, Lark K, Barker D (1984) Modeling of dynamic material behavior in hot deformation: forging of Ti-6242. Metall Trans A 15:1883–1892

[55] Prasad Y, Seshacharyulu T (1998) Processing maps for hot working of titanium alloys. Mater Sci Eng A 243(1–2):82–88

[56] Zhang C, Lian Y, Chen Y et al (2019) Hot deformation behavior and microstructure evolution of a TiBw/near α-Ti composite with fine matrix microstructure. Metals 9(4):481

[57] Ozerov M, Klimova M, Kolesnikov A, Stepanov N, Zherebtsov S (2016) Deformation behavior and microstructure evolution of a Ti/TiB metal–matrix composite during high-temperature compression tests. Mater Des 112:17–26. https://doi.org/10.1016/j.matdes.2016.09.051

[58] Zhang R, Huang L, Zhao X, Geng L, Wang S, Jiang S, Jiao Y (2021) Influence of deformation parameters and network structure to the microstructure evolution and flow stress of TiBw/Ti64 composite. Mater Sci Eng A. https://doi.org/10.1016/j.msea.2021.140997

[59] Gaisin R, Imayev V, Imayev R (2017) Effect of hot forging on microstructure and mechanical properties of near α titanium alloy/TiB composites produced by casting. J Alloys Compd 723:385–394

[60] Qiu P, Li H, Sun X, Han Y, Huang G, Lu W, Zhang D (2017) Reinforcements stimulated dynamic recrystallization behavior and tensile properties of extruded (TiB+TiC+ La_2O_3)/Ti6Al4V composites. J Alloys Compd 699:874–881